Electrochemical and modelling study of ZrNbO alloys aged under high temperature and high pressure PWR simulated conditions

Duncan Peyret, Damien Kaczorowski, Milan Skocic, Bernard Tribollet, Vincent Vivier

Electrochemical and modelling study of ZrNbO alloys aged under high temperature and high pressure PWR simulated conditions

Duncan Peyret,[a, b] Damien Kaczorowski,[b] Milan Skocic,[c,*] Bernard Tribollet,[d] Vincent Vivier[a,*]

[a] *CNRS, Laboratoire de Réactivité de Surface, UMR 7197, Sorbonne Université, 4 Place Jussieu, Paris 75005, France*

[b] *Framatome Lyon Gerland, 2 rue Professeur Jean Bernard, 69007 Lyon, France*

[c] *Framatome Centre Technique, 30 boulevard de l'Industrie, 71200 Le Creusot, France*

[d] *CNRS, Laboratoire Interfaces et Systèmes Électrochimiques, UMR 8235, Sorbonne Université, 4 Place Jussieu, Paris 75005, France*

**Corresponding authors: vincent.vivier@sorbonne-universite.fr; milan.skocic@framatome.com*

Abstract

This work proposes a kinetic study of Zirconium alloy when working under controlled temperature and pressure conditions to simulate pressurized water reactor (PWR) conditions. A detailed analysis of the experimental results allowed to describe each time constant observed on the impedance diagrams. A model based on the PDM including the anodic and cathodic reactions and the description of the interfacial capacitance is proposed and allows to fit the experimental results. Even if the overall oxide film formed on the alloy can reach several micrometers in thickness, only a compact oxide sub-layer of a few nanometers contributes to the impedance response.

Keywords:

ZrNbO alloy; Electrochemical impedance spectroscopy; Kinetic model

1. Introduction

Zirconium-niobium-oxygen alloys are widely used in pressurized water reactors (PWRs) for fuel cladding because of their low neutron absorption cross section, good corrosion resistance in nominal conditions, high melting point, and good mechanical properties. The fuel cladding is the first confinement barrier between the nuclear fuel and its products, and the coolant water. During their use in PWR, ZrNbO alloys inevitably exhibit corrosion due to environmental exposure. Therefore, understanding the corrosion mechanisms of ZrNbO alloys, and modelling and predicting the oxidation behaviour are essential for the nuclear industry to predict long-term behaviour of these materials.

The good corrosion resistance of zirconium alloys is linked to the formation of a passive film on its surface. Chen et al. [1] demonstrated through the use of Mott-Schottky plots, the electronic characteristic of a zirconium passive film aged at 250°C and 62 bars in $0.1\ \mathrm{M}\ \mathrm{B(OH)_3} + 0.001\ \mathrm{M}\ \mathrm{LiOH}$ solution deaerated with argon. This film presents an n-type electronic character, which shows that the predominant defects are oxygen or hydrogen vacancies and/or interstitial zirconium.

Generally, the oxide growth for zirconium alloys is composed of three steps, pre-transition, transition, and post-transition with a uniform corrosion. In pre-transition, the formed oxide is dense, and has a growth that follows a parabolic to a cubic trend resulting in monoclinic and tetragonal oxides. The oxide growth is accompanied by the growth of stress in the oxide. This stress arises due to the difference in volume between the oxide and the metal, characterised by a Pilling-Bedworth ratio of about 1.56. When this stress exceeds the critical thickness limit of the oxide and the oxide resistance drops due to crack formation, transition occurs, and the post-transition period arises. during the post-transition step, the oxide growth rate accelerates then remains constant. Oxide formed in post-transition is mainly porous, and composed of monoclinic oxide [2]–[4].

Impedance measurements of zirconium alloys have been extensively used to study the corrosion behaviour of these materials and characterize the passive film formed on the surface [4]–[8]. Interpretation of the impedance data have shown two rate-limiting processes: an anodic one limited by the transport of oxygen, and a cathodic one related to the reduction of an oxidant in solution. To further analyse the impedance data, equivalent electrical models have been developed, based on the understanding of the interfaces, consisting of common electrical analogue elements (resistor, capacitor and constant phase element, Warburg element) [4], [9],

[10]. However, it is often difficult to describe precisely the electrochemical and physicochemical processes only in terms of an association of electrical elements. The combination of electrical equivalent circuits with impedance models that account for the electrochemical and chemical reactions can provide a finer description of the material reactivity [11]–[13].

Different models have already been used for describing the oxidation process of zirconium alloys, such as the mixed-conduction model [14], [15] used to model Zr-1%Nb alloys in water cooled - water moderated energy reactor (WWER - 16 ppm K as KOH, 1400 ppm B as H_3BO_3 and 1 ppm Li as $LiOH$) simulated conditions around 300°C, in which they successfully used electrochemical impedance spectroscopy to develop a new model of oxide growth including the effect of a compressive stress. Independently, the Stefan model [16] has been used to model the oxidation and the hydriding processes of zirconium alloys in light water reactor (LWR, encompasses pressurized water reactors and boiling water reactors) simulated conditions at 327°C in order to account for moving boundaries for a fine description of the oxide growth involving 2 interfaces.

In the case of a thin oxide film, an impedance model based on the Point Defect Model (PDM) developed by Macdonald [12] is often suggested. For instance, Ai et al. [11] devised an impedance model for zirconium alloys aged at 250°C and 62 bar in $0.1\ \mathrm{M\ B(OH)_3} + 0.001\ \mathrm{M\ LiOH}$ solution for 24 hours at different applied potentials. These zirconium alloys have two oxide layers, an inner dense layer and an outer porous layer. The electrical equivalent circuit is composed of two loops in series, where each loop corresponds to a time constant. The authors determined that the porous oxide layer dominates the corrosion resistance of zirconium alloys aged at 250°C in aqueous deaerated solution.

The aim of this work is to examine the corrosion mechanisms of ZrNbO alloys aged in simulated PWR conditions by electrochemical experimental analysis and by modelling the involved processes. Special attention will be paid to the reduction reaction and mass transport of species related to this reaction since they should act as rate-limiting steps for zirconium corrosion in the experimental conditions chosen. A model is developed to reflect our understanding of zirconium corrosion, adapted from the PDM of Macdonald [12] and from other studies too [11], [17]–[19]. The oxide thickness evolution obtained from electrochemical impedance spectroscopy (EIS) analysis is also reported and discussed. The first part of this article introduces the impedance model, whereas the second part presents the experimental

results of corrosion. Finally, the interpretation of the applied model on experimental data is discussed.

2. Model describing the oxide film formation as a function of time

2.1. Model assumptions

Mostly the same assumptions are employed in this paper as the ones used by Chao et al. [18] for describing the oxide film formation. It is assumed that:

(a) a continuous oxide film is formed when the external potential is nobler than the Flade potential [20](refers to the step from the passive region to the active region) and that the alloy dissolution is controlled by the Zr dissolution, only;

(b) this oxide incorporates a high concentration of oxygen vacancies, zirconium interstitials, electrons, and electron holes;

(c) there is no interaction between defects;

(d) the electrical field inside the thin film is independent of its thickness;

(e) the rate-determining step when an electron is involved in physicochemical reactions is located either at the metal/oxide interface or at the oxide/solution interface, whereas the predominant step of a process that involves oxygen vacancies is their transport through the oxide film;

(f) the interfaces can be polarized, hence, the potential difference at those interfaces depends on both the applied potential and the pH of the solution;

(g) the impedance measurements do not affect the thickness of the oxide film;

(h) the experimental measurements are performed only in deaerated solution.

2.2. Kinetic model

The model devised in this work relies on the work of Ai et al. [11], Sharifi-Asl et al. [17], Bojinov et al. [19] and the Macdonald's Point Defect Model [12]. Our approach consists in considering the different anodic and cathodic contributions, as well as the dielectric properties of the interface. This leads us to propose an equivalent electrical circuit in which each element is described by an analytical expression which depends on the physicochemical reactions of the system and not a simple assembly of elements (R, C, L) whose only objective is to fit the impedance diagram.

Figure 1 (A) pictures the description of the two interfaces at which the reactions that are envisioned to occur in the system. Reaction (1) is responsible for injecting Zr_i^{4+} in the oxide film at the metal/oxide interface and for oxidation of metal zirconium. This reaction is reversible which allows to take into account the transport of charged species in the film. Reaction (2) corresponds to the oxidation of zirconium metal and leads to the growth of the oxide film at the metal/oxide interface with the transport of oxygen vacancies through the oxide thickness. At the oxide/solution interface, interstitial zirconium combines with water and is released into the solution as described by Reaction (3). Reaction (4) results in the consumption of oxygen vacancies by the reduction of water and Reaction (5) describes the dissolution of the oxide film. Reaction (6) corresponds to the reduction reaction of the solvent, namely the proton reduction reaction in this case. Reaction (2) and reaction (5) are the reactions that produce or consume the oxide, respectively. These reactions thus control the oxide growth or oxide thinning.

In this description of the zirconium corrosion, only reactions (1) and (2) can be realized in the two directions. This introduces, in the equation of the system's current, the defects' concentrations (as described below by Eq.(8)). The defects' concentrations can then be linked to the defects' transport, which can occur *via* diffusion and migration. Thus, Nernst-Planck equations was solved to calculate the defects' concentrations.

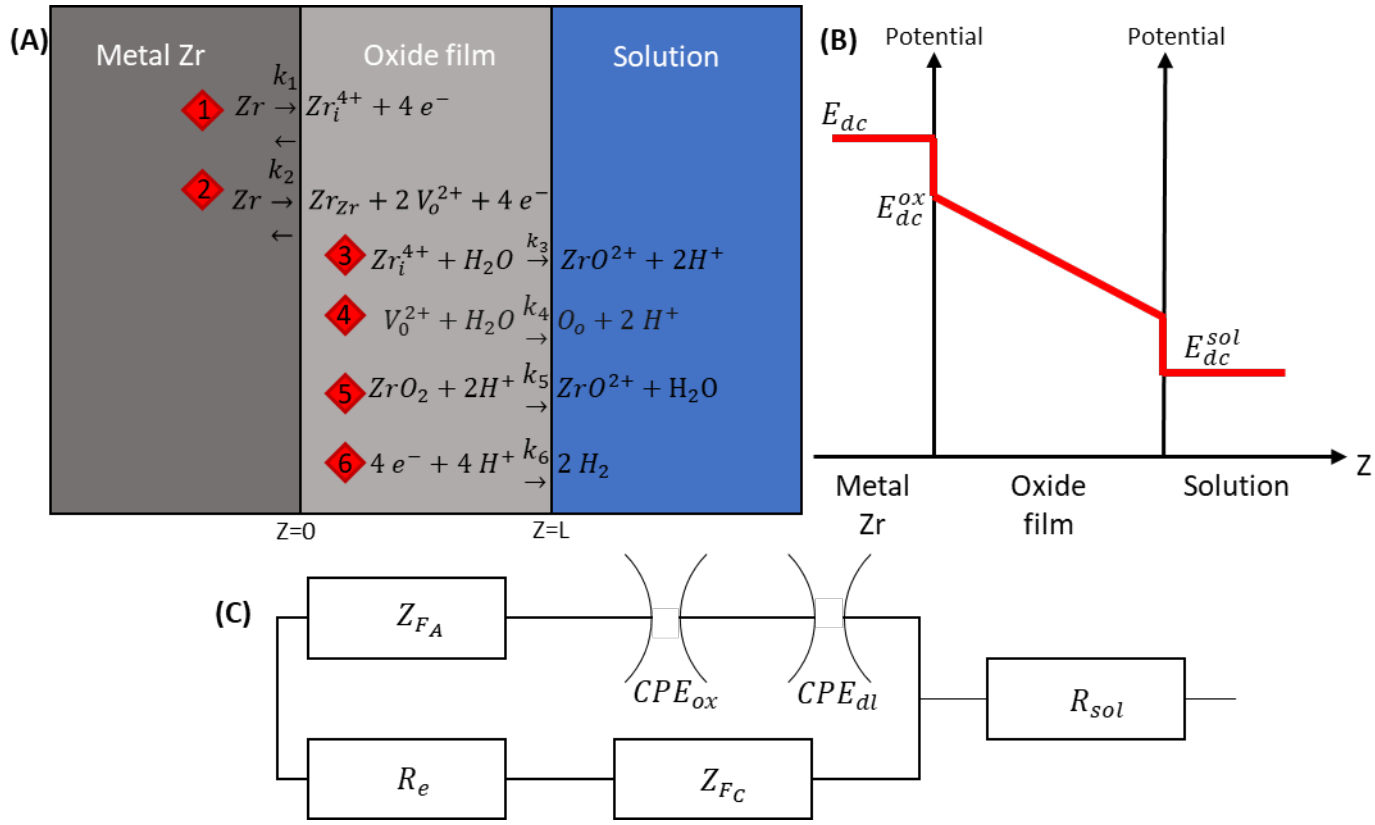

Figure 1 : Schematic representation of (A) corrosion processes describing ZrNbO alloys, exhibiting the reactions taken into account in the developed model ; Zr = zirconium atom in metal, Zr_i^{4+} = zirconium anion interstitial, Zr_{Zr} = zirconium metal cation in the film, V_O^{2+} = oxygen anion vacancy, O_O = oxygen in the film; (B) Potential evolution through the oxide thickness, demonstrating that each part of the interface exhibits different potentials; E_{dc} = applied direct potential on metal zirconium, E_{dc}^{ox} = potential at metal /oxide interface, E_{dc}^{sol} = potential at oxide/solution interface; (C) Electrical circuit describing ZrNbO alloys, used in the developed model ; Z_{F_A} = anodic faradaic impedance, CPE_{ox} = oxide capacitance, CPE_{dl} = double layer capacitance, R_e = electron transport resistance, Z_{F_C} = cathodic faradaic impedance, R_{sol} = solution resistance.

The interfacial reaction rate constants k_i are assumed to be potential dependant and function of the oxide film thickness. Assuming that the oxide film is made of a double oxide layer composed of an inner dense oxide and an outer porous oxide, the ohmic drop influences the interfacial reaction rate constants. The resistance of this porous oxide layer, R_{ext}, is a function of its resistivity, ρ_{ox}, its thickness, δ_{ext}, and its porosity P according to

$$R_{ext} = \frac{\rho_{ox}\delta_{ext}}{P} \qquad (1)$$

The rate constants of the reactions sketched in Figure 1 (A) are defined as follows

$$k_i = k_i^0 e^{a_i(V - IR_{ext}) + b_i\delta_{ox} + C_i pH} \quad i = 1,2 \qquad (2)$$

$$k_{-1} = k_1^0 e^{a_{-1}(V - IR_{ext}) + b_{-1}\delta_{ox} + C_{-1}pH} \quad (3)$$

$$k_{-2} = k_2^0 e^{a_{-2}(V - IR_{ext}) + b_{-2}\delta_{ox} + C_{-2}pH} \quad (4)$$

$$k_i = k_i^0 e^{C_i pH} \quad i = 3, 4, 5 \quad (5)$$

$$k_6 = k_6^0 e^{a_6(V - IR_{ext}) + C_6 pH} \quad (6)$$

where V is the electrode potential, I the DC component of the current flowing through the electrode, δ_{ox} the inner oxide film thickness, k_i^0 the standard rate constant for the reaction i, and a_i, b_i and C_i are coefficients for the rate constants. To simplify the resolution of the system, we assume that pH at oxide/solution interface remains constant and that the term comprising its contribution is included in the standard reaction rate constant.

The potential applied corresponds to the potential difference between the metal electrode and the reference electrode (V), but the potential of interest which corresponds to the potential used for the electrochemical reaction is the potential difference between the dense oxide/porous oxide interface and the reference electrode (U). These two potentials can be linked to the potential drop due to the porous oxide as

$$U = V - IR_{ext} \quad (7)$$

In the following, we have replaced Eq.(7) in the rate constants, and we assume having only a dense oxide, since neglecting the porous oxide film can be justified by EIS data analysis (as presented in section 4.2). This assumption opposes the conclusion of Ai. et al [11], where they determine that it is the outer oxide layer that dominates corrosion resistance.

The potential variation in the electrochemical system varies as shown in Figure 1 (B), where a potential drop occurs at the metal/oxide interface and at the oxide/solution interface. An ohmic drop is also present in the oxide. When a small variation in potential is applied to the metal, for example when an impedance measurement is performed, this is reflected throughout the system, and it is assumed that this difference remains the same at all points.

All interfacial reactions that produce or consume electrons contribute to the total current density. In the system presented in Figure 1, the anodic faradaic current represents the electron contribution with transport of ions, whereas the cathodic faradaic current represents the electron contribution for reactions without transport of ions in oxide thickness. Using the Butler-Volmer equation, the anodic current is given as

$$I_{F_A} = nFA\left\{k_1 + k_2 - \left[C_{Zr_i^{4+}}(0)k_{-1} + C_{V_O^{2+}}^2(0)k_{-2}\right]\right\} \quad (8)$$

where F is Faraday's constant, n the number of electrons exchanged per reaction, A the samples surface, $C_{Zr_i^{4+}}(0)$ the concentration of interstitial zirconium at the metal/oxide interface, and $C_{V_o^{2+}}(0)$ the concentration of oxygen vacancies at the metal/oxide interface. The activity for metal zirconium and Zr_{Zr} in Reaction (1) and Reaction (2) are assumed to be equal to unity.

The total derivative of Eq. (8) when applying a sinusoidal perturbation $\delta x = \Delta x e^{j\omega t}$, with x representing I_{F_A}, U, δ_{ox}, $C_{Zr_i^{4+}}(0)$ or $C_{V_o^{2+}}(0)$, expresses as

$$\frac{\Delta I_{F_A}}{nFA} = I_U \Delta U + I_{\delta_{ox}} \Delta \delta_{ox} + I_{Zr}^0 \Delta \mathrm{C}_{\mathrm{Zr_i^{4+}}}(0) + I_V^0 \Delta C_{V_o^{2+}} \qquad (9)$$

where

$$I_U = a_1 k_1 + a_2 k_2 - \left[a_{-1} k_{-1} C_{Zr_i^{4+}}(0) + a_{-2} k_{-2} C_{V_o^{2+}}^2(0)\right] \qquad (10)$$

$$I_{\delta_{ox}} = b_1 k_1 + b_2 k_2 - \left[b_{-1} C_{Zr_i^{4+}}(0) k_{-1} + \mathrm{b}_{-2} C_{V_o^{2+}}^2(0) k_{-2}\right] \qquad (11)$$

$$I_{Zr}^0 = -k_{-1} \qquad (12)$$

$$I_V^0 = -2 k_{-2} C_{V_o^{2+}}(0) \qquad (13)$$

The mass balance for the oxide film thickness is obtained from Reaction (2) and Reaction (5), which allow to express the time evolution of the film thickness as

$$\frac{d\delta_{ox}}{dt} = \Omega k_2 - \Omega k_5 - \Omega \mathrm{k}_{-2} C_{V_o^{2+}}^2(0) \qquad (14)$$

where Ω is the volume per mole of cations in the oxide film. Thus, the total derivative of this expression allows to express the change in thin oxide film thickness as

$$\Delta \delta_{ox} = \alpha_{\delta_{ox}} \Delta U + \beta_{\delta_{ox}} \Delta \mathrm{C}_{\mathrm{V_o^{2+}}}(0) \qquad (15)$$

$$\alpha_{\delta_{ox}} = \frac{\Omega[\mathrm{a}_2 k_2 - a_{-2} k_{-2} C_{V_o^{2+}}^2(0)]}{j\omega - \Omega[b_2 k_2 - b_{-2} k_{-2} C_{V_o^{2+}}^2(0)]} \qquad (16)$$

$$\beta_{\delta_{ox}} = \frac{\Omega}{j\omega - \Omega[b_2 k_2 - b_{-2} k_{-2} C_{V_o^{2+}}^2(0)]} \left[-2 k_{-2} C_{V_o^{2+}}(0)\right] \qquad (17)$$

The transport of interstitials and vacancies is governed by both diffusion and migration. The Nernst-Planck equations expressed as

$$J_i = -D_i \frac{\partial C_i(Z)}{\partial Z} - 2 D_i k C_i(Z) \qquad (18)$$

$$\frac{\partial C_i(Z)}{\partial t} = D_i \frac{\partial^2 C_i(Z)}{\partial Z^2} + D_i q_i K \frac{\partial C_i(Z)}{\partial Z} \qquad (19)$$

where i corresponds to either Zr_i^{4+} or V_o^{2+}, J is the current density, D_i the diffusion coefficient, q_i is the number of charges, $K = \frac{F}{RT}\epsilon$ with R being the ideal gas constant (8.31 $J.mol^{-1}.K^{-1}$), T the temperature (K), ϵ the electric field strength ($V.cm^{-1}$), and $k = \frac{q_i K}{2}$.

By solving differential Eq. (18) and Eq.(19) for $C_{V_o^{2+}}(0)$, we obtain:

$$\Delta C_{V_o^{2+}}(0) = \Delta C^0_{V_o^{2+}U}\Delta U + \Delta C^0_{V_o^{2+}\delta_{ox}}\Delta\delta_{ox} \qquad (20)$$

By solving differential Eq. (18) and Eq.(19) for $C_{Zr_i^{4+}}(0)$, it comes

$$\Delta C_{Zr_i^{4+}}(0) = \Delta C^0_{Zr_i^{4+}{}_U}\Delta U + \Delta C^0_{Zr_i^{4+}{}_{\delta_{ox}}}\Delta\delta_{ox} \qquad (21)$$

The derivation of Eq.(20) and Eq. (21) are presented in Annexe A.

Substitution of Eq.(20), Eq. (21) and Eq. (15) into Eq. (9) yields the anodic faradaic admittance corresponding to the anodic contribution:

$$Y_{F_A} = \frac{\Delta I_{F_A}}{\Delta U} = nFA\{I_U + I_{\delta_{ox}}OX + I^0_{Zr}\left[\Delta C^0_{Zr_i^{4+}U} + \Delta C^0_{Zr_i^{4+}\delta_{ox}}OX\right] + I^0_{V_o}[\frac{\Delta C^0_{V_o^{2+}U}\left[1-\beta_{ox}\Delta C^0_{V_o^{2+}\delta_{ox}}\right] + \Delta C^0_{V_o^{2+}\delta_{ox}}\alpha_{ox} + \beta_{ox}\Delta C^2_{V_o^{2+}\delta_{ox}}}{1-\beta_{ox}\Delta C^0_{V_o^{2+}\delta_{ox}}}]\} \qquad (22)$$

$$OX = \frac{\alpha_{ox} + \beta_{ox}\Delta C^0_{V_o^{2+}\delta_{ox}}}{1-\beta_{ox}\Delta C^0_{V_o^{2+}\delta_{ox}}} \qquad (23)$$

Similarly, using the Butler-Volmer equation allows the cathodic faradaic current to be defined as:

$$I_{F_C} = nFA\{-k_6\} \qquad (24)$$

The total differential of Eq. (24) by applying a sinusoidal perturbation $\delta x = \Delta x e^{j\omega t}$, with x representing I_{F_C}or U, can be presented, in the cathodic faradaic admittance form, as:

$$Y_{F_C} = -nFAa_6k_6 \qquad (25)$$

No physico-chemical reactions for the porous oxide layer are represented in Figure 1 (A), since the impedance measurement only analyses the dense oxide film (as presented in section 4.2). However, the resistance of the porous layer must be considered, since the current circulates through it.

The calculation of these different analytical expressions describing the impedance of the system requires knowledge of interstitial and vacancy concentrations at metal/oxide interface. Bojinov et al. [19] provided analytical expressions for the concentration of point defects involved in the electrochemical reactions (1) to (6) which are assumed to be governed by the generalised transport equations established by Fromhold and Cook [21]

$$J_i = -D_i \frac{\partial C_i}{\partial Z} \cosh\left(\frac{zFaU}{RT}\right) - \frac{D_i}{a} C_i * \sinh\left(\frac{zFaU}{RT}\right) \quad (26)$$

Where i corresponds to either Zr_i^{4+} or V_o^{2+}, z is the charge of species, and a the atomic jump distance. Assuming that the high field approximation holds, i.e., ($\frac{zFaE}{RT} \gg 1$, $\tanh\left(\frac{zFaE}{RT}\right) = 1$) and $\sinh\left(\frac{zFaE}{RT}\right) = \frac{e^{\frac{zFaE}{RT}}}{2}$, Eq. (26) thus expresses as

$$J_i = -D_i' \frac{\partial C_i}{\partial Z} - \frac{D_i'}{a} C_i \quad (27)$$

with $D' = \frac{D}{2} e^{\frac{zFaE}{RT}}$. By solving Eq.(27) for interstitial zirconium and oxygen vacancies, one obtains the general form presented in Annexe B. The defect concentrations appearing in impedance equations are only located at the metal/oxide interface, thus:

$$C_{Zr}(0) = E_{Zr} - \frac{B_{Zr}}{A_{Zr}} \frac{a}{D'_{Zr}} \quad (28)$$

$$C_{V_o}(0) = A_{V_o} + B_{V_o} \quad (29)$$

The total impedance of the system includes the anodic impedance contribution, the cathodic impedance contribution, and the resistance of the solution, R_{sol}, presented in Figure 1 (C). The anodic impedance branch is composed of the impedance due to physico-chemical reactions, the anodic faradaic impedance (Z_{F_A}) in series with the oxide capacitance (CPE_{ox}) and the double layer capacitance (CPE_{dl}). The cathodic branch is in parallel with the anodic branch and is composed of an electron transport impedance (R_e) in series with the cathodic faradaic impedance (Z_{F_C}). Therefore, the total impedance of the system presented in Figure 1 (C) is

$$Z = \frac{1}{\frac{1}{Z_A} + \frac{1}{Z_C}} + R_{sol} \quad (30)$$

where:

$$Z_A = Z_{F_A} + \mathrm{Z_{CPE_{ox}}} + \mathrm{Z_{CPE_{dl}}} \quad (31)$$

$$Z_C = R_e + Z_{F_C} \quad (32)$$

$Z_{CPE_{ox}}$ and $Z_{CPE_{dl}}$ are the impedance of constant phase elements for the oxide layer and the double layer, respectively. The impedance equation of a constant phase element is as

$$Z_i = \frac{1}{Q_i(\omega j)^{\alpha_i}} \quad (33)$$

With Q_i and α_i being parameters of the constant phase element and i standing for $_{ox}$ or $_{dl}$.

The use of a CPE for describing the oxide film capacitance is helpful from a practical point of view. However, its physical meaning is limited unless one is able to evaluate the properties of the film (resistivity, permittivity) and propose an expression for impedance base on these properties, such as a power law distribution of the resistivity or the Yong model as discussed in detail in [22].

It is important here to underline that this equivalent circuit (Figure 1 C) contains in fact all the kinetics of the processes involved in the corrosion of zirconium.

3. Experimental

3.1. Samples and solution

The samples used are zirconium alloys in cylindrical shape composed of 1.0 wt% of niobium and 0.12 wt% of oxygen, supplied by Framatome, France. The samples were cleaned in an ultrasonic bath first in acetone, then in ethanol, and finally in pure water for 15 minutes each.

The experimental solution simulating PWR coolant was composed of 1.5 ppm of lithium and 650 ppm of bore. This solution was deaerated with argon to decrease the oxygen content down to 10 ppb. The oxygen content is measured with a Hach orbisphere 510.

3.2. Electrochemical measurements

Two autoclaves were used to characterise electrochemically our samples, a static autoclave, and a dynamic autoclave (*i.e.,* an autoclave coupled to a recirculating loop for the electrolyte circulating at a flow rate of 0.35 L/min). Nominal experimental conditions were at 360±5°C and 190±5 bar. A platinum wire and a home-made Ag/AgCl electrode were used as reference electrodes, the body of the autoclave was used as counter electrode, and the zirconium sample was used as working electrode. The electrochemical setup included the EchemLab xm Solartron analytical or Modulab Solartron analytical potentiostat.

Impedance measurements were performed at the open circuit potential (OCP), at +100 mV vs OCP and at -100 mV vs OCP on a frequency domain ranging from 1 MHz to 10 mHz with 13 points per frequency decade and with an excitation signal of 25 mV amplitude. Polarization curves were measured anodically and cathodically, from -10 mV vs OCP to +250 mV vs OCP and from +10 mV vs OCP to -250 mV vs OCP, respectively, with a scan rate of 0.167 mV/s. Measurement of the open circuit potential was carried out for the duration of the experiment, except while impedance or polarization measurements were underway.

3.3. Validation of experimental impedance data

Kramers-Kronig transformations [23] have been used to check the consistency of the EIS measurements. Transformed real and imaginary components greatly coincide with experimental data, except at low frequency. This is ascribed to the fact that impedance data are measured on a finite frequency domain, whereas the transformations are defined on an infinite frequency domain and the data at low frequency are not always well defined due to the experimental conditions (corrosion behaviour at 360°C and 190 bar). At long exposure times, impedance at low frequencies do not tend to a finite value, thus behaving similarly to a semi-infinite Warburg.

4. Results and discussion

4.1. Impedance results

A typical impedance spectrum of ZrNbO alloy aged at 360°C and 190 bar in PWR solution for 13 days in a dynamic autoclave is shown in Figure 2, in form of a Nyquist plot. ZrNbO alloys have first a parabolic oxide growth, then a linear oxide growth at high temperature and high pressure, with oxide thicknesses increasing rapidly to the order of a micron [8], [24]. Figure 2 shows a well-defined impedance diagram for a measurement realized in these conditions, thus the system seems to be stable enough during the whole duration of the measurement. Three time-constants can be observed on the Nyquist plot. The first time constant at high frequencies corresponds to an artefact due to the experimental setup, which is also obtained in Vermoyal's work [8]. This signal is an impedance response since it fulfils Kramers-Kronig relations. However, the use of an electrical circuit instead of the electrochemical system allowed to measure the same high frequency time constant, thus validating the analysis. It should be noted that the experimental constraints related to the measurement at high pressure and high temperature do not allow to modify certain aspects of the experimental device and the choice was made to keep this device but to correct the measurements concerning this contribution that

we were able to independently evaluate experimentally. The second flattened semi-circle at medium frequencies describes the electronic behaviour limitation of the system comprising the contribution of the oxide resistance, the charge transfer resistance, and the oxide capacitance. The low-frequency time constant is attributed to a transport behaviour since there is a 45° angle at the beginning of the loop, whereas the low frequency tends towards a real value, thus suggesting transport process in a layer of finite thickness.

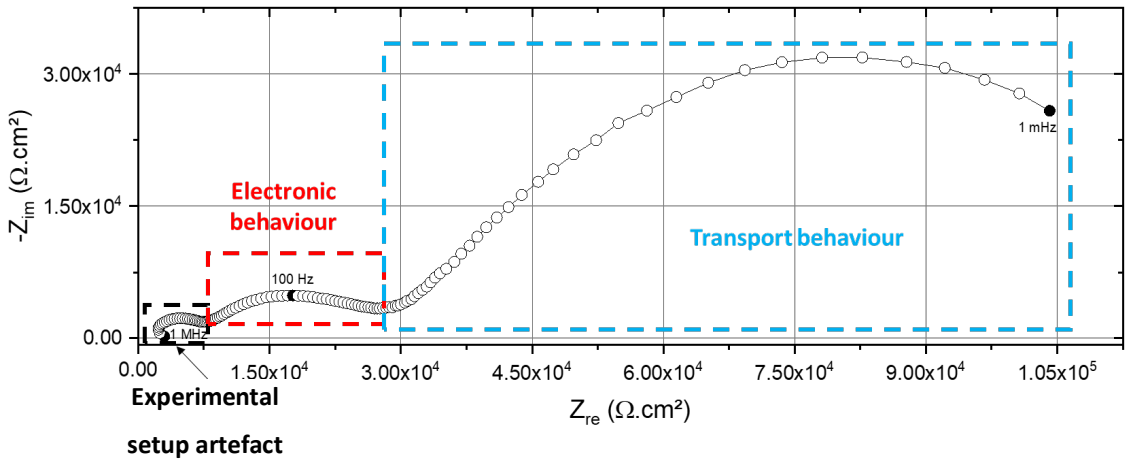

Figure 2 : Typical Nyquist plot of ZrNbO alloys at OCP in a frequency range of 1 MHz to 1 mHz aged at 360°C, 190 bar and in PWR solution for 13 days.

To ascertain whether the transport limitation observed on the impedance diagram corresponds to a transport process in solution or in the oxide film, a dynamic autoclave was used which was adapted and developed by Skocic [25]. This dynamic autoclave allows to modulate the flow of the solution circulating around the samples and thus potentially modify the low-frequency impedance response if it is due to a contribution in solution. EIS measurements for three different flows at 280°C and 70 bar in PWR solution were performed as shown in Figure 3. At low frequency, a slight difference appears between the three plots. This difference is not sufficient to be ascribed to a change in the size of the diffusion layer and has instead been attributed to temperature gradients being significantly different between measurements due to the difference in solution fluxes. Hence, transport in solution is negligible, and the transport highlighted in the impedance measurements takes place in the oxide for ZrNbO alloys.

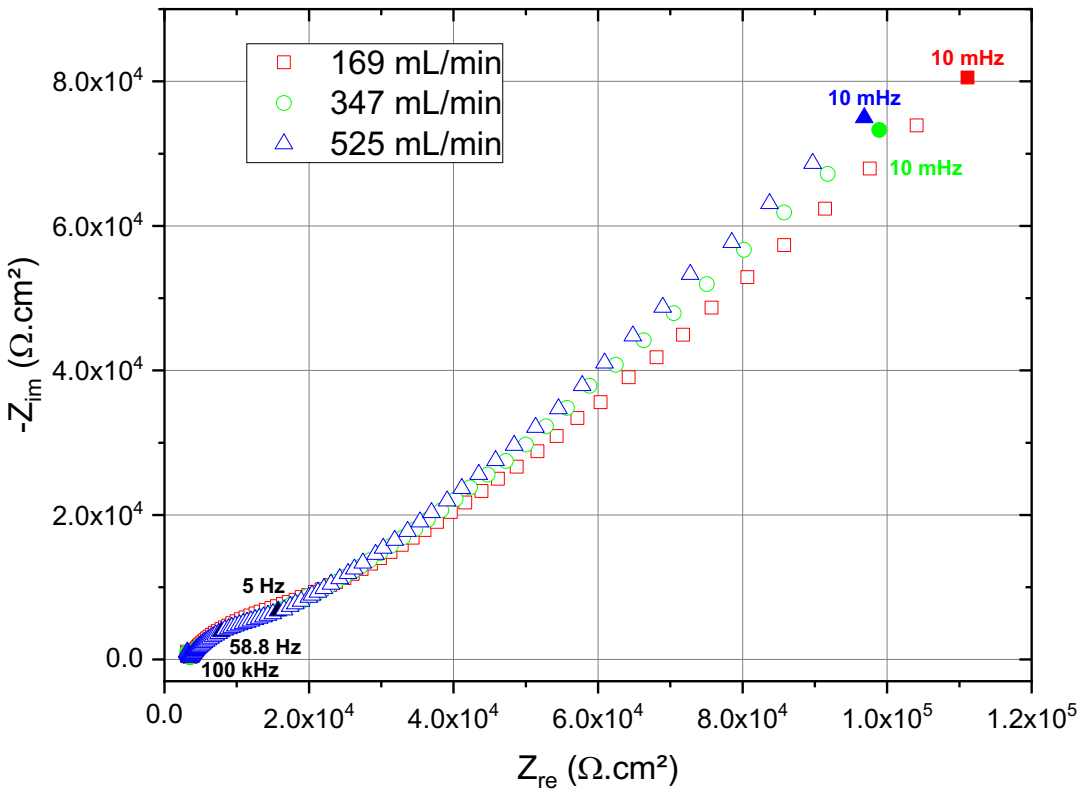

Figure 3: EIS measurements performed for three different flows of the solution at 280°C and 70 bar in PWR solution at the OCP in a dynamic autoclave having a 150 mm² cross section.

Polarization curves performed on two identical samples aged at 360°C and 190 bar for 7 days are presented in Figure 4 in an aerated solution corresponding to about 1 750 ppm O_2 (red circles) and in an oxygen-free solution (blue squares), both in a static autoclave. In the deaerated environment, a significant shift of the corrosion potential towards more negative values and a corrosion current smaller by about two orders of magnitude compared to the experiment performed in the presence of oxygen is observed. Moreover, at the end of the experiment, the oxide thickness of those samples was measured with an optical microscope. The oxide thickness of the sample from the aerated environment was 1.5 times larger than the oxide thickness of the sample studied in deaerated environment. These results show the primordial role of oxygen on the corrosion of zirconium and the thickening of the oxide layer for short immersion times.

The impedance response (Nyquist plots) of identical samples in different environments also shows differences, as shown in Figure 5. These measurements were performed on two identical samples aged at 360°C and 190 bar for 14 days and 59 days in an aerated solution (circles) and in an oxygen-free solution (squares), both in a static autoclave. The sample in an aerated solution shows a lower impedance than the sample in a deaerated solution, therefore, in aerated

solution, the sample corrodes faster than the deaerated sample, which is consistent with the polarization curves presented in Figure 4.

Moreover, EIS diagrams presented in Figure 5, show that the two samples behave differently. At 14 days, only one flat semi-circle seems to be present for the sample in aerated medium. Whereas at 59 days, the behaviour of the sample in aerated medium tends to the behaviour observed for sample in deaerated medium. This change of behaviour may be attributed to oxide transition.

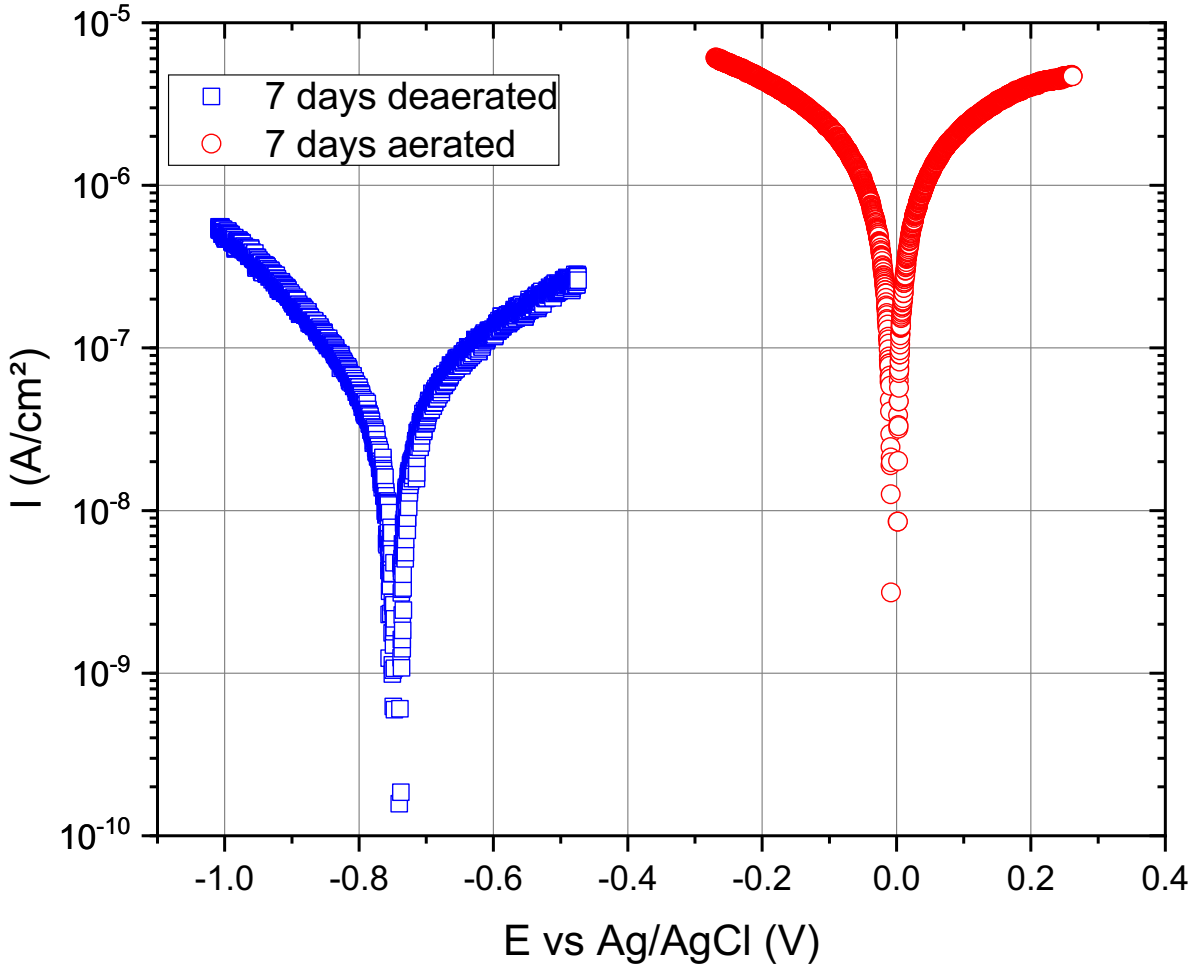

Figure 4: Polarization measurements of the same ZrNbO alloy aged at 360°C and 190 bar in PWR solution for 7 days, one in deaerated solution (□) and the other in aerated solution (○) (~1 750 ppm O_2).

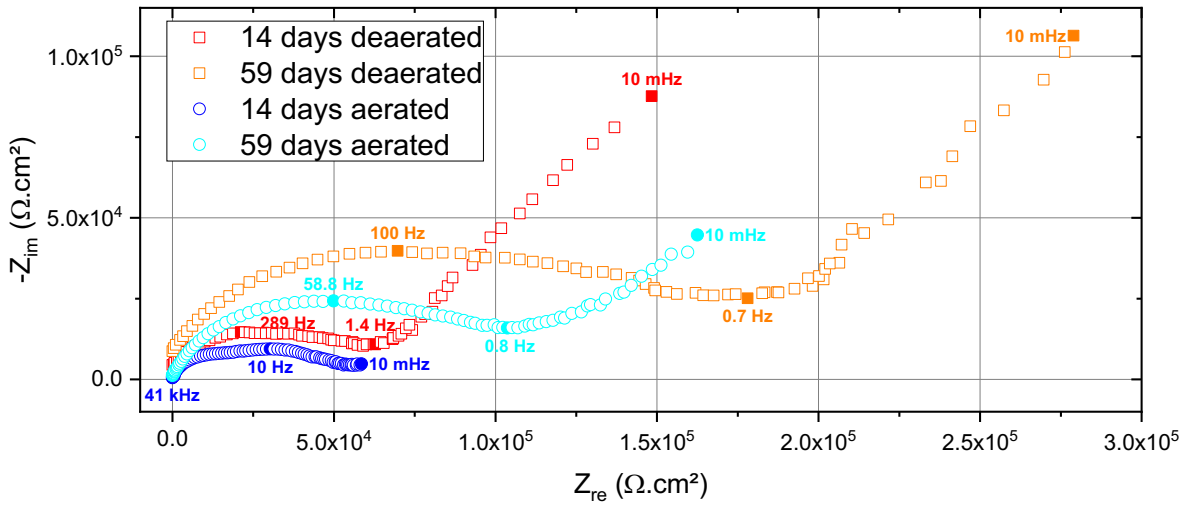

Figure 5: Corrected Nyquist plots (without the experimental setup artefact) for identical ZrNbO samples, one in a deaerated PWR solution (□) and the other in an aerated PWR solution (○); aged at 360°C and 190 bar for 14 days and 59 days.

Figure 6 shows impedance measurements performed at the OCP, and around the OCP, namely at -100 mV vs OCP (cathodically) and at +100 mV vs OCP (anodically) for two oxide thicknesses. The oxide thicknesses were calculated as a function of the alloy and the time and conditions of exposure in the autoclave, based on the charts presented in the work of Vermoyal [8]. The present measurements were performed on a ZrNbO alloy aged at 360°C and 190 bar in PWR solution contained in a static autoclave, resulting in 1 µm and 1.9 µm thick oxide films on the Zr alloy at 19 days of exposure and 52 days of exposure, respectively. An example of SEM and TEM observation of the oxide and the metal/oxide interface is presented on Figure 7 for a sample after 52 days exposure.

The cathodic measurements present the lowest impedance compared to OCP and anodic measurements for the two oxide thicknesses. It is thus concluded that the cathodic reactions contribute to the impedance response. Indeed, Motta et al. [26] have reported that proton reduction is the main cathodic reaction involved in zirconium corrosion, arguing that the hydrogen observed in zirconium metal comes primarily from hydrogen generated by the corrosion reaction. However, it should also be remembered that the role of oxygen is not necessarily negligible, as shown by the results previously discussed.

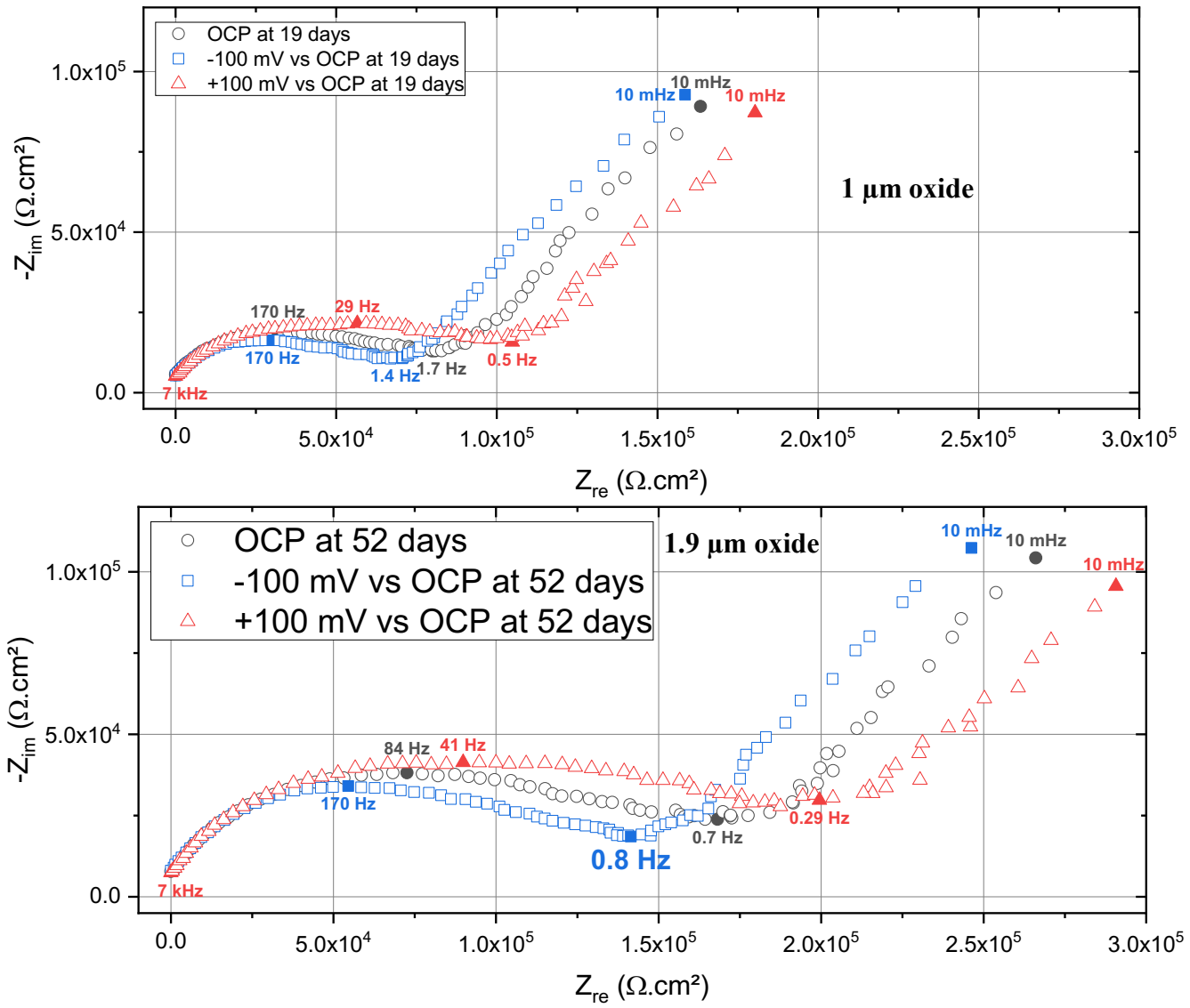

Figure 6: Corrected Nyquist plots (without the experimental setup artefact) obtained at the OCP (○), -100 mV vs OCP (□) and +100 mV vs OCP (▲) for two oxide thicknesses (1 µm and 1.9 µm) aged at 360°C and 190 bar in PWR solution for 19 days and 52 days; Represented oxide thicknesses are theoretical ones based on the work of Vermoyal [8].

The experimental temperature of 360°C has been used in previous studies [8], [27], [28], but other temperatures are investigated in order to characterize zirconium alloys, as such the work of Renciukova et al. in which experiments were performed at 340°C [4], Müller et al. who studied the corrosion of Zr alloy at 343°C and 400°C [29], or Ai et al. who performed experiments at 250°C [11]. The influence of the temperature on the impedance response of the ZrNbO alloy is presented in Figure 8 in a Nyquist representation. A ZrNbO sample with 0.7±0.1 µm oxide thickness was used for measurements realized in Figure 8 a & b. In Figure 8 c, the measurement realized at 300°C was on a ZrNbO sample aged for 15 days, and for the measurement at 360°C, another ZrNbO sample aged at 18 days is used.

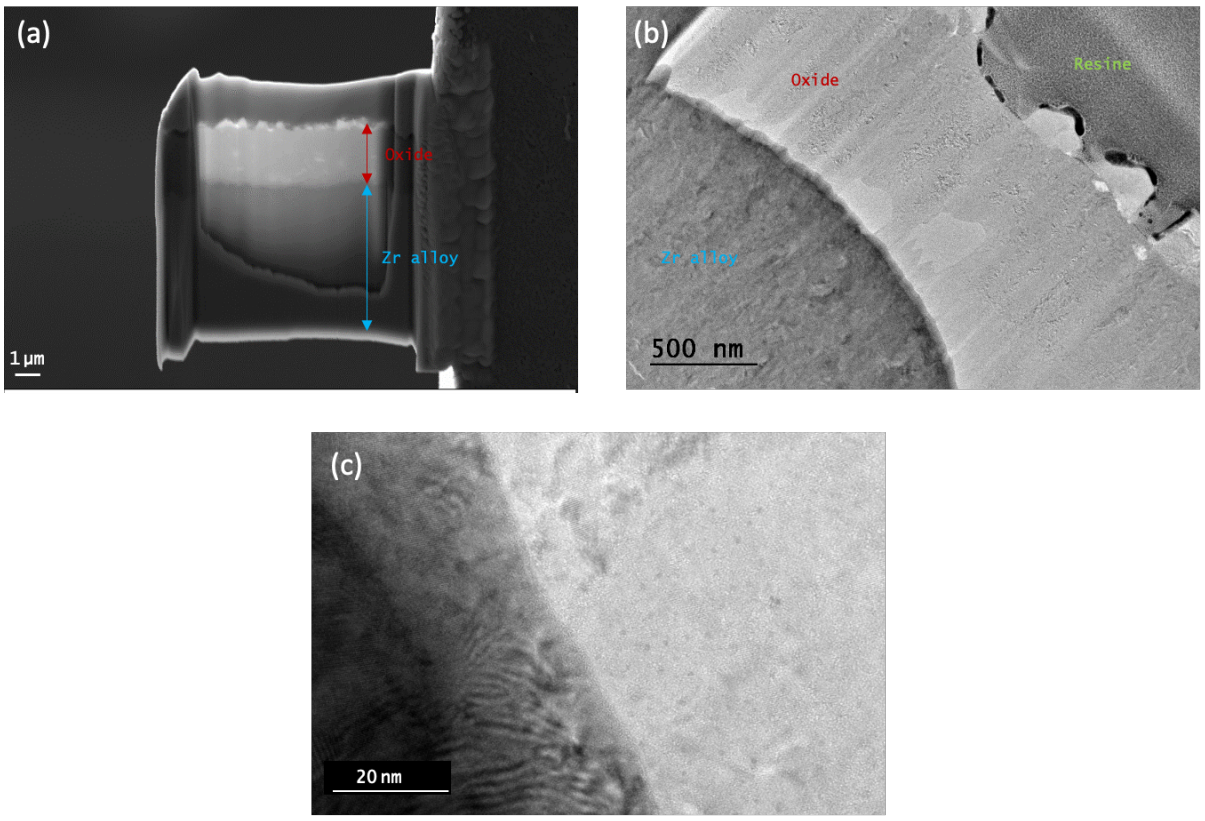

Figure 7: (a) SEM image of a FIB slide of a ZrNbO alloy oxidized at 360°C and 190 bar in a PWR medium at OCP for 52 days; (b) large scale TEM image of the oxide film; HRTEM at the interface metal/oxide.

For the lowest temperatures (Figure 8 a), the impedance diagrams show only one constant which is assimilated to a CPE behaviour with values of the modulus of impedance that are very large. Such a behaviour is characteristic of the dielectric response of the oxide layer on the material, and the kinetics of the electrochemical processes is very much slowed down. When the temperature is increased (Figure 8 b & c), the shape of the diagrams presented previously is gradually found, whereas the modulus of the impedance decreases, which is equivalent to a larger current density. This indicates that the temperature allows to activate the kinetics of the electrochemical reactions, and we observe therefore the time constants related to the charge transfer and the transport process.

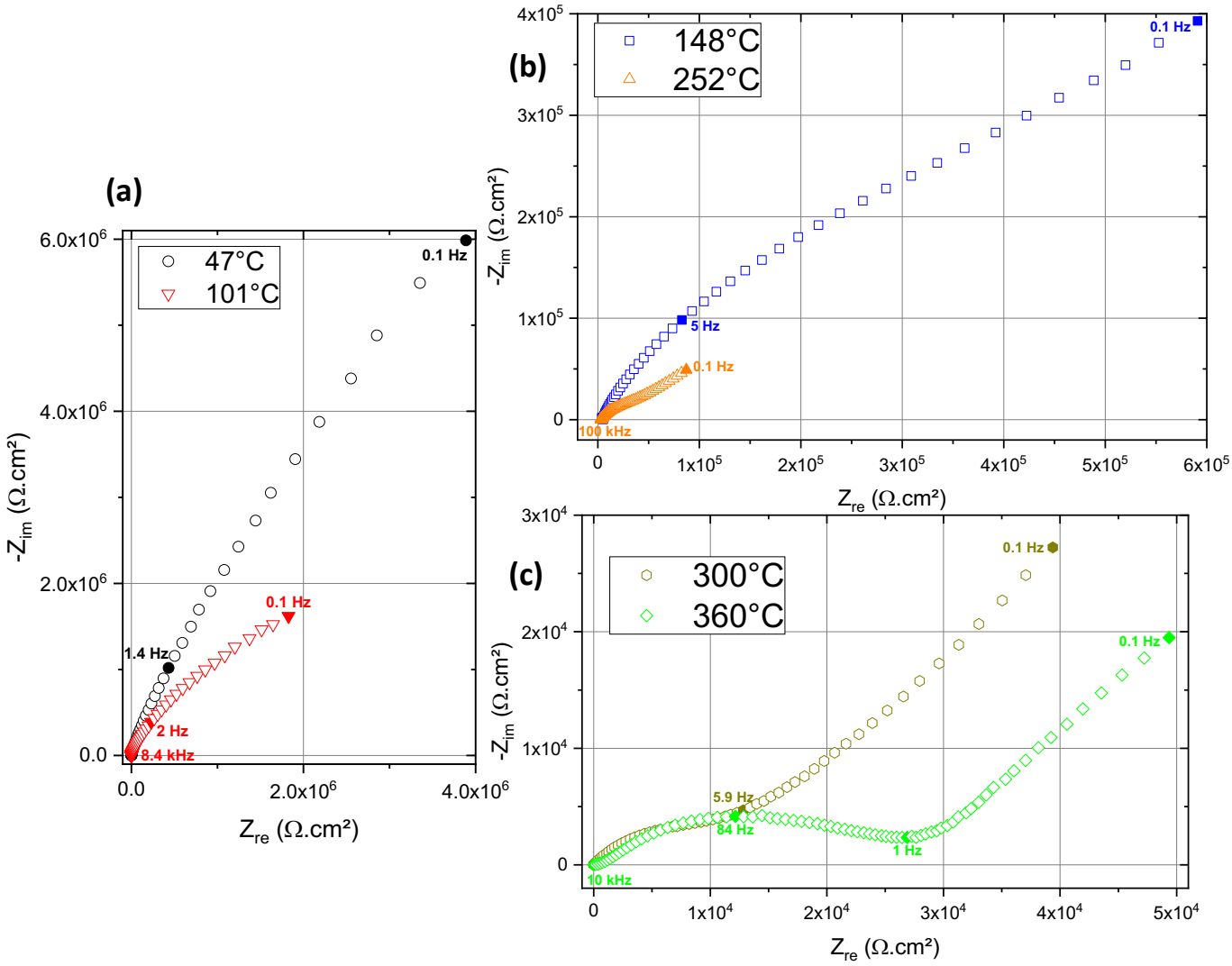

Figure 8: Corrected Nyquist plots of ZrNbO alloy realized at different experimental temperatures in PWR solution at a pressure granting a liquid phase to the solution; (a) and (c) measurements are realized on a ZrNbO sample having a 0.7±0.1 µm oxide thickness, measurement at 300°c is realized on another ZrNbO sample aged for 15 days (~1 µm oxide), measurement at 360°C is realized on another ZrNbO sample aged for 18 days (~1 µm oxide).

4.2. The porous oxide layer

The influence of the oxide layer thickness on the electrochemical response of the system was studied by comparing electrochemical measurements performed on ZrNbO alloys prepared in two different ways: one sample was pre-oxidized to an oxide thickness of 27 µm in a static autoclave at 360°C and 190 bar in a PWR solution, the second one was pre-oxidized to an oxide thickness of 1 µm in a static autoclave at 360°C and 190 bar in a PWR solution. Figure 9 shows the two EIS measurements performed on these materials. The sample with a 1 µm thin oxide shows only a dense oxide, whereas the sample with 27 µm thick oxide is characterized by both dense and porous oxide layers. In both cases, the EIS response exhibits two well-defined time

constants, one in the high frequency range (with a characteristic frequency of about 100 Hz) and a second one in the low frequency domain (in the mHz range).

The sample with a 27 µm thick oxide shows a higher impedance than the 1 µm thin oxide sample, therefore, a 27 µm thick oxide sample corrodes slower than a 1 µm thin oxide sample. The modulus of their impedance is of the same order of magnitude while having such a big oxide thickness difference, thus, it is not necessary that the impedance measurement analyses the total thickness of the oxide. The thick oxide sample is composed of two oxide layers; hence impedance measurement could analyse only the inner dense oxide layer.

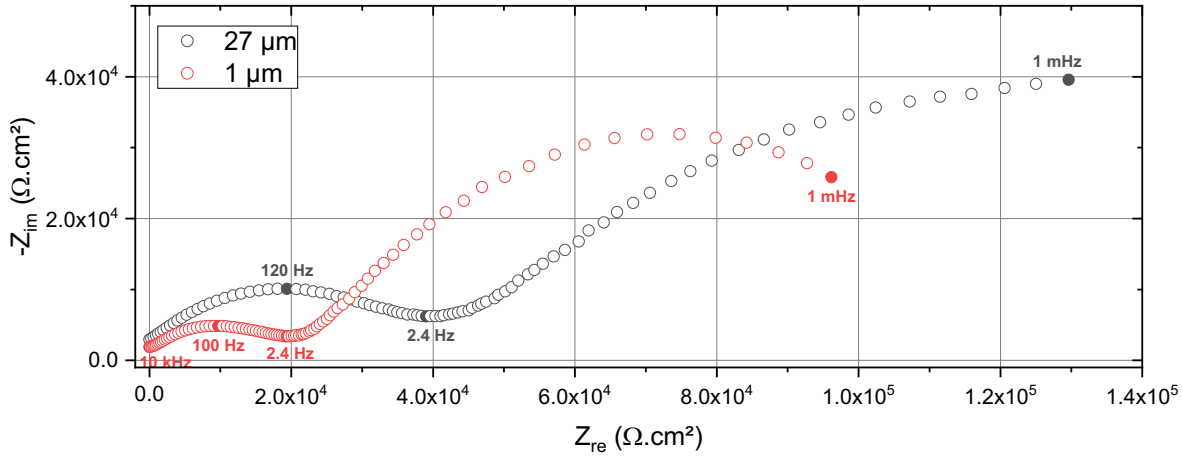

Figure 9 : Corrected Nyquist plot for the same ZrNbO alloys at OCP in PWR solution aged at 360°C and 190 bas for 13 days (1 µm of oxide) and for 2 473 days (27 µm of oxide).

4.3. Model results

To further exploit the impedance measurements, a model was developed based on the analysis presented in Section 2.2. The impedance diagrams have been fitted with this model with the use of a home-made software. However, given the number of parameters, it seems appropriate to set several parameters, especially using data from the literature. These parameters are reported in Table 1.

Table 1 : Fixed parameter values used in our model.

Parameter	Value/units	Source

T	$633.14\ K$	Experimental-this work
n	4	This work
a	$3.35 * 10^{-8} cm$	[30]
A	$70\ cm^2$	Experimental-this work
E_{app}	$-0.196\ V\ vs\ Pt$	Experimental-this work
Ω	$21.06\ cm^3.mol^{-1}$	[11]

Figure 10 presents the comparison between the obtained fit and the experimental data in Nyquist plot and Bode plots, for a measurement performed after 2 days of exposure. From this figure, the model fits fairly well with the experimental data. This fit seems to have a level of agreement similar to that reported in different studies [11], [31]. Hence, the impedance model developed provides a reasonable understanding of the experimental data for the early stages of corrosion.

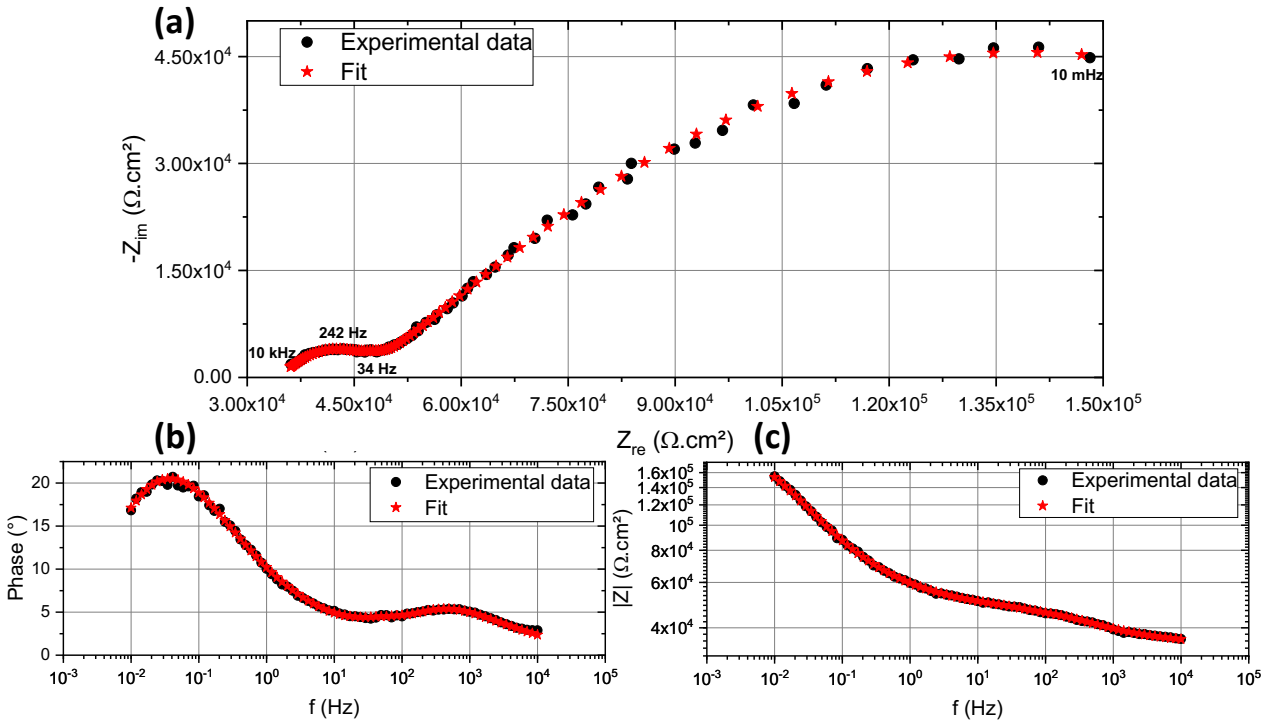

Figure 10 : Comparison of simulated data (★) and experimental data (●) of ZrNbO alloy at 360°C and 190 bar in PWR solution in the form of (a) a Nyquist plot, (b) the module and (c) the phase, after 2 days of exposure.

Table 2 presents the parameter values obtained by optimization of the model on experimental impedance data for measurement performed after 2 days of exposure. On the diffusion coefficients side, oxygen vacancy diffusion is faster than interstitial zirconium diffusion even

with important incertitude, which is in agreement with the literature [26]. As for the electron transport resistance, its value is 1 to 2 orders of magnitude lower than the system's value, thus it doesn't limit the corrosion process. Finally, the oxide thickness value is completely different to the total oxide thickness of the sample estimated at ~0.9 µm, based on the work of Vermoyal [8]. The oxide thickness calculated tends to be similar to the thickness of a sub-oxide. Hu et al. [32] reported that for a ZrNbO alloy with a few micrometres of oxide, sub-oxide thickness varies from ~60 nm up to ~350 nm. In our case, the oxide thickness isn't as thick as for Hu et al. but the order of magnitude of the oxide thickness found by them is of the order of magnitude of our calculated oxide thickness. This sub-oxide layer is thought to be formed while a slow oxidation takes place with the presence of a dense oxide layer [33]. As our oxide hasn't been through transition, confirmed visually by the oxide colour, our oxide has a predominantly dense oxide and slow oxidation kinetics. Thus, our oxide should have a sub-oxide layer. The sub-oxide layer is composed of a region of ZrO_x elements and of metal zirconium saturated in oxygen [32].

Table 2 : Parameter values of the developed model on the experimental impedance data for ZrNbO alloys in PWR solution at 360°C and 190 bar at OCP for 2 days of exposure.

Parameter	Value / unit
k_1^0	$6.9 * 10^{-2} \pm 1 * 10^{-3}\ mol.s^{-1}.cm^{-2}$
k_2^0	$4.2 * 10^{-6} \pm 4 * 10^{-7}\ mol.s^{-1}.cm^{-2}$
k_3	$2.13 * 10^{-3} \pm 1 * 10^{-5}\ mol.s^{-1}.cm^{-2}$
k_4	$2.7 * 10^{-1} \pm 3 * 10^{-2}\ mol.s^{-1}.cm^{-2}$
k_6^0	$4 * 10^{-14} \pm 4 * 10^{-13}\ mol.s^{-1}.cm^{-2}$
a_1	$51.046 \pm 0.006\ V^{-1}$
a_{-1}	$-60.89 \pm 0.06\ V^{-1}$
a_2	$97.9 \pm 0.3\ V^{-1}$
a_{-2}	$-90.4 \pm 0.4\ V^{-1}$
a_6	$-3 \pm 1 * 10^3\ V^{-1}$
b_1	$-5622 \pm 10\ cm^{-1}$
b_{-1}	$-9.51 * 10^3 \pm 10\ cm^{-1}$
b_2	$-8.3 * 10^3 \pm 1 * 10^2\ cm^{-1}$
b_{-2}	$-4 * 10^3 \pm 5 * 10^5\ cm^{-1}$
δ_{ox}	$6.2 * 10^{-7} \pm 1 * 10^{-8}\ cm$
$Q_{CPE_{ox}}$	$6 * 10^{-5} \pm 3 * 10^{-5}$
$\alpha_{CPE_{ox}}$	0.8 ± 0.3
$Q_{CPE_{dl}}$	$3 * 10^{-5} \pm 1 * 10^{-5}$

$\alpha_{CPE_{dl}}$	0.41 ± 0.07
R_{sol}	$3.44 * 10^4 \pm 2 * 10^2\ \Omega.cm^2$
R_e	$6 * 10^1 \pm 1 * 10^8\ \Omega.cm^2$
$D_{V_o^{2+}}$	$1.13 * 10^{-7} \pm 8 * 10^{-9}\ cm^2.s^{-1}$
$D_{Zr_i^{4+}}$	$5 * 10^{-12} \pm 1 * 10^{-12}\ cm^2.s^{-1}$
ϵ	$4.088 * 10^5 \pm 3 * 10^2\ V.cm^{-1}$

5. Conclusions

In the present work, an impedance model based on the point defect model for the growth of oxide layers formed on ZrNbO alloys under high temperature and high pressure deaerated aqueous solution conditions is developed, and an exploration of the electrochemistry of these aged alloys is presented.

The electrochemical exploration performed presents the importance of working at 360°C, at which the limiting processes are the most observable. These limiting processes are the transport of species in the oxide layer and a reduction reaction. Supposedly the transport of oxygen vacancies and the proton reduction are the limiting steps of ZrNbO oxidation. This seems to be in accordance with the simulated data of the developed impedance model that comprises those limiting steps.

The developed impedance model links electrochemical reactions, chemical reactions, diffusion of species, migration of species and the concentration of those moving species to form a coherent understanding of the ZrNbO oxidation system. Calculated parameters have reasonable values. The oxide value seems to represent mostly a sub-oxide thickness rather than the total oxide thickness, which would mean that impedance measurements would analyse the sub-oxide thickness, only.

Annexe A

By solving differential Eq. (18) and Eq.(19) for $C_{V_o^{2+}}(0)$, we obtain:

$$\Delta C_{V_o^{2+}}(0) = \Delta C^0_{V_o^{2+}U}\Delta U + \Delta C^0_{V_o^{2+}\delta_{ox}}\Delta\delta_{ox} \quad (34)$$

$$\Delta C^0_{V_o^{2+}U} = \frac{b_{1U}a_{21} - b_{1U}a_{22}}{a_{11}a_{22} - a_{12}a_{21}} \quad (35)$$

$$\Delta C^0_{V_o^{2+}\delta_{ox}} = \frac{b_{1L}a_{21} - b_{1L}a_{22}}{a_{11}a_{22} - a_{12}a_{21}} \quad (36)$$

$$a_{11} = r_1 D_{V_o^{2+}} + 2D_{V_o^{2+}}k - 2C_{V_o^{2+}}(0)k_{-2} \quad (37)$$

$$a_{12} = r_2 D_{V_o^{2+}} + 2D_{V_o^{2+}}k - 2C_{V_o^{2+}}(0)k_{-2} \quad (38)$$

$$a_{21} = e^{r_1 L}\left[D_{V_o^{2+}}r_1 + 2D_{V_o^{2+}}k + k_4\right] \quad (39)$$

$$a_{22} = e^{r_2 L}\left[D_{V_o^{2+}}r_2 + 2D_{V_o^{2+}}k + k_4\right] \quad (40)$$

$$b_{1U} = k_2 a_2 - k_{-2}a_{-2}C^2_{V_o^{2+}}(0) \quad (41)$$

$$b_{1L} = b_2 k_2 - b_{-2}k_{-2}C^2_{V_o^{2+}}(0) \quad (42)$$

$$r_1 = -k + \sqrt{k^2 + \frac{j\omega}{D_{V_o^{2+}}}} \quad (43)$$

$$r_2 = -k - \sqrt{k^2 + \frac{j\omega}{D_{V_o^{2+}}}} \quad (44)$$

By solving differential Eq. (18) and Eq.(19) for $C_{Zr_i^{4+}}(0)$, it comes

$$\Delta C_{Zr_i^{4+}}(0) = \Delta C^0_{Zr_i^{4+}{}_U}\Delta U + \Delta C^0_{Zr_i^{4+}{}_{\delta_{ox}}}\Delta\delta_{ox} \quad (45)$$

$$\Delta C^0_{Zr_i^{4+}{}_U} = \frac{f_{1U}e_{21} - f_{1U}e_{22}}{e_{11}e_{22} - e_{12}e_{21}} \quad (46)$$

$$\Delta C^0_{Zr_i^{4+}{}_L} = \frac{f_{1L}e_{21} - f_{1L}e_{22}}{e_{11}e_{22} - e_{12}e_{21}} \quad (47)$$

$$e_{11} = r_3 D_{Zr_i^{4+}} + 2D_{Zr_i^{4+}}k - k_{-1} \quad (48)$$

$$e_{12} = r_4 D_{Zr_i^{4+}} + 2D_{Zr_i^{4+}}k - k_{-1} \quad (49)$$

$$e_{21} = e^{r_3 L}\left[r_3 D_{Zr_i^{4+}} + 2D_{Zr_i^{4+}}k + k_3\right] \quad (50)$$

$$e_{22} = e^{r_4 L}\left[r_4 D_{Zr_i^{4+}} + 2D_{Zr_i^{4+}}k + k_3\right] \quad (51)$$

$$f_{1U} = a_1 k_1 - a_{-1}k_{-1}C_{Zr_i^{4+}}(0) \quad (52)$$

$$f_{1L} = b_1 k_1 - b_{-1}k_{-1}C_{Zr_i^{4+}}(0) \quad (53)$$

$$r_3 = -k' + \sqrt{k'^2 + \frac{j\omega}{D_{Zr_i^{4+}}}} \quad (54)$$

$$r_4 = -k' - \sqrt{k'^2 + \frac{j\omega}{D_{Zr_i^{4+}}}} \quad (55)$$

Where $k' = \frac{q_{Zr_i^{4+}K}}{2}$ and L is the oxide thickness.

Annexe B

As the fluxes of the defects are related to reactions presented on Figure 1 (A), the boundary conditions can be defined as:

$$J_{Zr_i^{4+}}(Z=0) = k_1 - k_{-1}C_{Zr}(0) \quad (56)$$

$$J_{Zr_i^{4+}}(Z=L) = k_3 C_{Zr}(L) \quad (57)$$

$$J_{V_o^{2+}}(Z=0) = k_2 - k_{-2}C_{V_o}^2(0) \quad (58)$$

$$J_{V_o^{2+}}(Z=L) = k_4 C_{V_o}(L) \quad (59)$$

The steady state solutions for Zr_i^{4+} and V_o^{2+} of Eq. (27), coupled with the boundary conditions (Eqs.(56), (57) and (58), (59)), are:

$$C_{Zr} = E_{Zr}e^{-\frac{Z}{a}} - \frac{B_{Zr}}{A_{Zr}}\frac{a}{D'_{Zr}} \quad (60)$$

$$C_{V_o} = A_{V_o}e^{-\frac{Z}{a}} + B_{V_o} \quad (61)$$

With:

$$A_{Zr} = 1 + \frac{D'_{Zr}e^{-\frac{L}{a}}}{k_{-1}(D'_{Zr} + k_3 a)} - \frac{ae^{-\frac{L}{a}}}{D'_{Zr} + k_3 a} \quad (62)$$

$$B_{Zr} = \frac{k_1 D'_{Zr}e^{-\frac{L}{a}}}{k_{-1}(D'_{Zr} + k_3 a)} \quad (63)$$

$$E_{Zr} = \frac{k_1}{k_{-1}} + \frac{B_{Zr}a}{A_{Zr}D'_{Zr}} - \frac{B_{Zr}}{A_{Zr}k_{-1}} \quad (64)$$

$$A_{V_o} = \frac{-1 + \sqrt{1 + 4a_{V_o}k_2}}{2a_{V_o}} e^{\frac{L}{a}}\left[\frac{1}{k_4} + \frac{a}{D'_{V_o}}\right] \quad (65)$$

$$B_{V_o} = \frac{1 - \sqrt{1 + 4a_{V_o}k_2}}{2a_{V_o}}\frac{a}{D'_{V_o}} \quad (66)$$

$$a_{V_o} = \frac{a^2 k_{-2}}{{D'_{V_o}}^2} - \frac{2k_{-2}a^2 e^{\frac{L}{a}}}{{D'_{V_o}}^2} - \frac{2k_{-2}ae^{\frac{L}{a}}}{D'_{V_o}k_4} + \frac{k_{-2}e^{\frac{2L}{a}}}{k_4^2} + \frac{k_{-2}a^2 e^{\frac{2L}{a}}}{{D'_{V_o}}^2} + \frac{2k_{-2}ae^{\frac{2L}{a}}}{D'_{V_o}k_4} \quad (67)$$

Eqs.(60) and (61) are the generalized defect concentrations equations.

References

[1] Y. Chen, M. Urquidi-Macdonald, et D. D. Macdonald, « The electrochemistry of zirconium in aqueous solutions at elevated temperatures and pressures », *Journal of Nuclear Materials*, vol. 348, nº 1, p. 133-147, janv. 2006, doi: 10.1016/j.jnucmat.2005.09.014.

[2] IAEA, « Corrosion of zirconium alloys in nuclear power plants », International Atomic Energy Agency, Vienna, IAEA-TECDOC-684, 1993.

[3] J. S. Moya, M. Diaz, J. F. Bartolomé, E. Roman, J. L. Sacedon, et J. Izquierdo, « Zirconium oxide film formation on zircaloy by water corrosion », *Acta Materialia*, vol. 48, nº 18-19, p. 4749-4754, déc. 2000, doi: 10.1016/S1359-6454(00)00267-6.

[4] V. Renciukova, J. Macak, P. Sajdl, R. Novotny, et A. Krausova, « Corrosion of zirconium alloys demonstrated by using impedance spectroscopy », *Journal of Nuclear Materials*, vol. 510, p. 312-321, 2018, doi: 10.1016/j.jnucmat.2018.08.005.

[5] T. Kim, A. Couet, S. Kim, Y. Lee, S. C. Yoo, et J. H. Kim, « In-situ electrochemical study of zirconium alloy in high temperature hydrogenated Water conditions », *Corrosion Science*, vol. 173, p. 108745, août 2020, doi: 10.1016/j.corsci.2020.108745.

[6] A. Krausová, J. Macák, P. Sajdl, R. Novotný, V. Renčiuková, et V. Vrtílková, « In-situ electrochemical study of Zr1nb alloy corrosion in high temperature Li + containing water », *Journal of Nuclear Materials*, vol. 467, p. 302-310, déc. 2015, doi: 10.1016/j.jnucmat.2015.10.005.

[7] J. Schefold, D. Lincot, A. Ambard, et O. Kerrec, « The Cyclic Nature of Corrosion of Zr and Zr-Sn in High-Temperature Water (633 K) », *Journal of The Electrochemical Society*, vol. 150, nº 10, p. B451, 2003, doi: 10.1149/1.1602079.

[8] J. J. Vermoyal, « Contribution a l'identification des processus cinetiquement limitants de l'oxydation des alliages de zirconium », Joseph Fourier, 2000.

[9] M. Kiran Kumar, S. Aggarwal, V. Kain, T. Saario, et M. Bojinov, « Effect of dissolved oxygen on oxidation and hydrogen pick up behaviour—Zircaloy vs Zr–Nb alloys », *Nuclear Engineering and Design*, vol. 240, nº 5, p. 985-994, mai 2010, doi: 10.1016/j.nucengdes.2009.12.021.

[10] Z. Zou, W. Xue, X. Jia, J. Du, R. Wang, et L. Weng, « Effect of voltage on properties of microarc oxidation films prepared in phosphate electrolyte on Zr–1Nb alloy », *Surface and Coatings Technology*, vol. 222, p. 62-67, mai 2013, doi: 10.1016/j.surfcoat.2013.01.059.

[11] J. Ai, Y. Chen, M. Urquidi-Macdonald, et D. D. Macdonald, « Electrochemical impedance spectroscopic study of passive zirconium », *Journal of Nuclear Materials*, vol. 379, nº 1-3, p. 162-168, sept. 2008, doi: 10.1016/j.jnucmat.2008.06.011.

[12] D. D. Macdonald, « Some personal adventures in passivity—A review of the point defect model for film growth », *Russian Journal of Electrochemistry*, vol. 48, nº 3, p. 235-258, mars 2012, doi: 10.1134/S1023193512030068.

[13] J. Ai, Y. Chen, M. Urquidi-Macdonald, et D. D. Macdonald, « Electrochemical Impedance Spectroscopic Study of Passive Zirconium », *Journal of The Electrochemical Society*, vol. 154, nº 1, p. C43, 2007, doi: 10.1149/1.2374946.

[14] M. Bojinov, W. Cai, P. Kinnunen, et T. Saario, « Kinetic parameters of the oxidation of zirconium alloys in simulated WWER water – Effect of KOH content », *Journal of Nuclear Materials*, vol. 378, nº 1, p. 45-54, août 2008, doi: 10.1016/j.jnucmat.2008.04.014.

[15] I. Betova, M. Bojinov, et V. Karastoyanov, « Long-Term Oxidation of Zirconium Alloy in Simulated Nuclear Reactor Primary Coolant—Experiments and Modeling », *Materials*, vol. 16, nº 7, 2023, doi: 10.3390/ma16072577.

[16] M. Reyes, A. Aryanfar, S. W. Baek, et J. Marian, « Multilayer interface tracking model of zirconium clad oxidation », *Journal of Nuclear Materials*, vol. 509, p. 550-565, oct. 2018, doi: 10.1016/j.jnucmat.2018.07.025.
[17] S. Sharifi-Asl, M. L. Taylor, Z. Lu, G. R. Engelhardt, B. Kursten, et D. D. Macdonald, « Modeling of the electrochemical impedance spectroscopic behavior of passive iron using a genetic algorithm approach », *Electrochimica Acta*, vol. 102, p. 161-173, juill. 2013, doi: 10.1016/j.electacta.2013.03.143.
[18] C. Y. Chao, L. F. Lin, et D. D. Macdonald, « A Point Defect Model for Anodic Passive Films: III . Impedance Response », *Journal of The Electrochemical Society*, vol. 129, nº 9, p. 1874-1879, sept. 1982, doi: 10.1149/1.2124318.
[19] M. Bojinov, G. Fabricius, T. Laitinen, K. Mäkelä, T. Saario, et G. Sundholm, « Coupling between ionic defect structure and electronic conduction in passive films on iron, chromium and iron–chromium alloys », *Electrochimica Acta*, vol. 45, nº 13, p. 2029-2048, mars 2000, doi: 10.1016/S0013-4686(99)00423-5.
[20] P. Lorbeer et W. J. Lorenz, « A critical consideration of the flade potential », *Corrosion Science*, vol. 21, nº 1, p. 79-86, janv. 1981, doi: 10.1016/0010-938X(81)90066-4.
[21] A. T. Fromhold Jr. et E. L. Cook, « Diffusion currents in large electrical fieldsfor discrete lattices », *Journal of Applied Physics*, vol. 38, p. 1546-1553, 1967.
[22] B. Tribollet, V. Vivier, et M. E. Orazem, « EIS Technique in Passivity Studies: Determination of the Dielectric Properties of Passive Films », in *Encyclopedia of Interfacial Chemistry*, 1st ed. Elsevier, 2018, pp. 93-107.
[23] M. E. Orazem et B. Tribollet, *Electrochemical impedance spectroscopy*. in The Electrochemical Society series. Hoboken (New Jersey): Wiley, 2008.
[24] V. V. Likhanskii et I. A. Evdokimov, « Review of theoretical conceptions on regimes of oxidation and hydrogen pickup in Zr-alloys », *TRINITI*, p. 17, 2008.
[25] M. Skocic, « Etude (photo)-électrochimique en réacteur simulé du phénomène de shadow corrosion des alliages de zirconium », Université Grenoble Alpes, 2016. [En ligne]. Disponible sur: https://tel.archives-ouvertes.fr/tel-01334030
[26] A. T. Motta, A. Couet, et R. J. Comstock, « Corrosion of Zirconium Alloys Used for Nuclear Fuel Cladding », *Annual Review of Materials Research*, vol. 45, nº 1, p. 311-343, juill. 2015, doi: 10.1146/annurev-matsci-070214-020951.
[27] A. T. Motta, M. J. G. da Silva, A. Yilmazbayhan, R. J. Comstock, Z. Cai, et B. Lai, « Microstructural Characterization of Oxides Formed on Model Zr Alloys Using Synchrotron Radiation », *JAI*, vol. 5, nº 3, p. 1-20, mars 2008, doi: 10.1520/JAI101257.
[28] M. Oskarsson, « Study on the Mechanisms for Corrosion and Hydriding of Zircaloy », Doctoral thesis, comprehensive summary, Materialvetenskap, Stockholm, 2000. Consulté le: 29 novembre 2000. [En ligne]. Disponible sur: http://urn.kb.se/resolve?urn=urn:nbn:se:kth:diva-3045
[29] S. Müller et L. Lanzani, « Corrosion of Zr-1Nb and Zr-2.5Nb in 0.1 M LiOH at 343°C », *Procedia Materials Science*, vol. 8, p. 46-55, 2015, doi: 10.1016/j.mspro.2015.04.047.
[30] K. Doi, « La structure atomique de ZrO2 amorphe », *Bulletin de Minéralogie*, p. 216-225, 1966.
[31] J. Ai, Y. Chen, M. Urquidi-Macdonald, et D. D. Macdonald, « Electrochemical Impedance Spectroscopic Study of Passive Zirconium », *Journal of The Electrochemical Society*, vol. 154, nº 1, p. C52, 2007, doi: 10.1149/1.2374947.
[32] J. Hu *et al.*, « Understanding corrosion and hydrogen pickup of Zr nuclear fuel cladding alloys-the role of oxide microstructure, porosity, suboxide and SPPs », p. 28.

[33] N. Ni *et al.*, « How the crystallography and nanoscale chemistry of the metal/oxide interface develops during the aqueous oxidation of zirconium cladding alloys », *Acta Materialia*, vol. 60, nº 20, p. 7132-7149, déc. 2012, doi: 10.1016/j.actamat.2012.09.021.